Exploring ocean circulation on icy moons heated from below

Suyash Bire[1], Wanying Kang[1], Ali Ramadhan[1], Jean-Michel Campin[1], John Marshall[1]

[1]Earth, Atmospheric, and Planetary Sciences, Massachusetts Institute of Technology, Cambridge, MA 02139 US

Key Points:

- Simulation of convection driven by uniform bottom heating on an idealized icy moon setup
- Dynamics are characterized in terms of non-dimensional numbers

Corresponding author: Suyash Bire, `bire@mit.edu`

Abstract

We numerically explore the convection and general circulation of an ocean encased in a spherical shell of uniform thickness which is heated from below by an imposed, spatially-uniform heat flux and whose temperature at the upper surface is relaxed to a constant temperature, imagined to be the freezing point of water. We describe the phenomenology and equilibrium solutions obtained across a broad range of two key non-dimensional numbers: the natural Rossby number, Ro^*, a measure of the influence of rotation, and $\eta = R/(R+H)$ where R is the radius of the moon and H the depth of its ocean, a measure of the geometry of the moon. Icy moons such as Europa and Enceladus are characterised by $Ro^* << 1$ and thus profoundly influenced by rotation and convective motions which align with the tangent cylinder. They also have a small η which determines the meridional extent of the tangent cylinder and delineates two distinct regimes of circulation — rolls and plumes which are prominent outside and inside the tangent cylinder, respectively. We attempt to rationalise amplitudes and scales of the circulation in terms of these two non-dimensional numbers and how the circulation changes with them. Finally, in parameter regimes appropriate to icy moons, we find that plumes are more efficient at transferring heat to the upper boundary, resulting in polar cooling. In the absence of plumes, for example in diffusive simulations in which they are suppressed, the rolls take over resulting in equatorial cooling.

Plain Language Summary

With subsurface oceans of icy moons of the Solar System emerging as hotspots for search for extraterrestrial life, it is important to understand the dynamics of these oceans. With this aim in mind, this study performs numerical simulations to understand how effective the rotation and geometry of the moon are in determining the nature of circulation in an idealized ocean heated from below. We express our results in terms of non-dimensional numbers, which could then be used to predict the nature of circulation in oceans of real icy moons provided their rotation rate, geometry, and bottom heating is well known. We also find that turbulence, which is often very hard to measure, cannot be overlooked.

1 Introduction

Icy moons with subsurface oceans, such as Enceladus (Thomas et al., 2016) and Europa (Hand & Chyba, 2007), are targets in the search for extraterrestrial life. Not only is there a liquid water ocean on these icy moons, but also the ocean appears to be salty (Postberg et al., 2009; Trumbo et al., 2019), indicating present or past interactions between the ocean and the silicate core beneath. Methane and macromolecular organic compounds have been detected in the sprays emanated from the geysers on the south pole of Enceladus (Postberg et al., 2018; Waite et al., 2006). Tholin, an abiotic organic compound that may facilitate prebiotic chemistry formation (Borucki et al., 2002) and provide food for heterotrophic microorganisms before autotrophy evolved (Stoker et al., 1990), has been found on the surface of Europa (Borucki et al., 2002). Such evidence suggest a very high astrobiological potential of icy moon worlds. However, our understanding of the physical and chemical processes going on in the ocean, ice shell, and silicate core are still very limited. Among all the puzzles that face us, ocean dynamics is of particular importance because it results in transport of nutrients, heat, salt, and potential biosignatures between the core to the ice shell.

The two major drivers of ocean circulation on icy moons are, first, bottom heating and, second, the salinity flux induced by freezing and melting of ice and the temperature variation just beneath the ice-shell due to the dependence of the freezing point of temperature on pressure. In this work, we will focus on the first and not address the second. Our goal is to explore how ocean dynamics depend on the depth, the heat flux prescribed at the bottom and the rotation rate of the moon. We do this by identifying key non-dimensional numbers that govern the dynamics. A further goal will be to explore how ocean dynamics carry heat coming in at the bottom up to the ice shell above, the resulting temperature distribution within the ocean, and the general circulation that is set up. Important context is provided by previous numerical studies of ocean circulation on icy moons (Soderlund et al., 2013; Soderlund, 2019; Amit et al., 2020), as well as explorations of convection in rotating, spherical shells (J. Aurnou et al., 2003, 2008; Dormy et al., 2004; Takehiro, 2008; Gastine et al., 2016). The modus operandi of all such studies is to identify key controlling non-dimensional parameters, perform experiments in parameter space that can be reached either numerically or in the laboratory, and then extrapolate from them to the regimes where icy moons are thought to exist. In previous studies the non-dimensional numbers employed are typically the Rayleigh number (Ra) and Ekman number (E), both of which depend on the eddy viscosity and diffusivity assumed in the model, and the temperature difference imposed across the water column. Appropriate values of Ra and E for icy moons are not known with any certainty because turbulent processes must be represented by eddy viscosities and diffusivities which are not distinct from the convective process itself.

Here, as discussed in detail below, we choose to characterize the fluid dynamics in terms of the natural Rossby number, Ro^* defined by:

$$Ro^* = \left(\frac{B}{f^3H^2}\right)^{1/2}, \tag{1}$$

which depends on B, the buoyancy flux being carried across the fluid, $f = 2\Omega$, the rotation rate, and H, the total depth of the convective layer. This leads to a tidy division of the controlling parameters between a rotational parameter independent of diffusion (Ro^*) and a viscous/diffusive parameter (E). This is especially useful for application to icy moons because, although Ro^* is somewhat constrained by observations, the Ra number is rather uncertain because, as noted above, it depends on poorly known values of eddy diffusivity and viscosity.

We find that Ro^* has great utility in organising our experiments and putting them in the context of likely flow regimes on icy moons. Moreover, we show that the intensity and spatial scale of turbulent motions and their efficiency of radial heat transport can be rationalized in terms of Ro^* across a vast range of Ro^* values, from very small (the icy moon regime) to large (more typical of convection on Earth's atmosphere).

The other non-dimensional parameter we employ is a measure of the geometry of the moon and in particular its tangent cylinder, $\eta = R/(R+H)$ where R is the radius of the moon and H the depth of its ocean. When η is close to unity the fluid shell is thin; as it decreases the fluid deepens and the influence of Taylor-Proudman and the tangent cylinder is felt over a larger meridional fraction of the spherical domain. When Ro^* is small and the ocean is deep, two distinct regions emerge demarcated by the tangent cylinder – upright convection occurs at higher latitudes inside the tangent cylinder, whereas roll-like 'Busse' convection (Busse, 1970) occurs in tropical latitudes outside of it.

Our paper is set out as follows. Section 2 sets up the problem and identifies key non-dimensional numbers: the (Ro^*, E) pairing and the geometrical factor η. We will have a particular interest in where Europa and Enceladus lie in this phase space. Section 3 describes the numerical strategy and boundary conditions employed. Rather than prescribe a temperature difference across the fluid we impose a heat flux at the lower boundary and relax the fluid to the freezing point of water at the upper boundary. Section 4 describes and interprets the solutions obtained as key non-dimensional numbers are changed. Finally, in Section 5, we summarize and conclude.

2 Convection in a rotating spherical shell driven by heating from below

What is the nature of the convective activity driven by heating from below in a deep spherical shell that comprises an icy moon? Under what circumstances is the convection rotationally-controlled so that Taylor-Proudman constraints dominate? What are the implications of those rotational constraints on the general circulation of an ocean in a deep spherical shell? As sketched in figure 1 the external parameters of our problem are the radius of the moon R, the depth of the ocean H, the rotation rate of the moon Ω and the buoyancy flux B emanating from the silicate core. These are all somewhat constrained by observations thus enabling us to place, for example, Enceladus and Europa in (Ro^*, η) phase space.

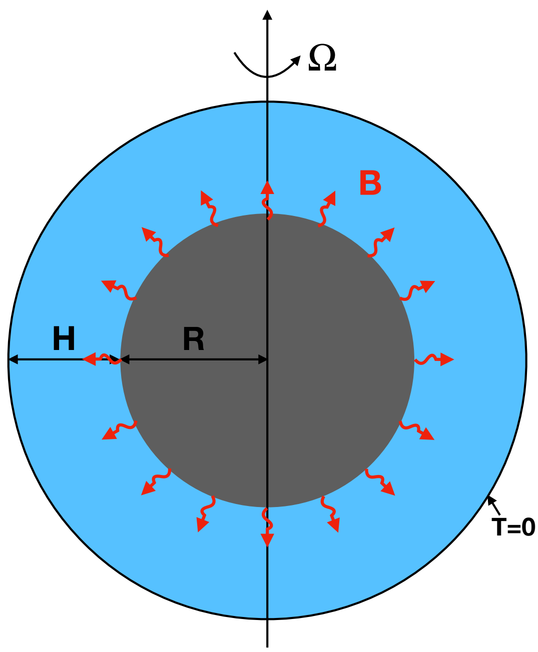

Figure 1. Geometry of the ocean of our icy moon. The grey region represents the silicate core of radius R which is enveloped by a liquid ocean, shown in blue, of depth H. The ice shell is the white exterior region and is not marked. The red arrows pointing radially outwards represent the imposed buoyancy flux B due to heating in the silicate core. The temperature at the upper boundary is relaxed to $0\,^\circ$C which leads to heat loss. The axis of rotation is along Ω. The two thin black lines mark the tangent cylinder. The geometrical parameters define η. We assume an equation of state in which the density only depends on the temperature linearly. This assumption, together with a specification of a (constant) gravitational acceleration, define Ro^*.

2.1 Scaling ideas

For clarity we begin by briefly reviewing key scaling ideas which will be used to frame our study. These are motivated by the literature on open ocean convection reviewed by Marshall and Schott (1999). Given that the timescale for fluid rising in a convective element from below on a small but deep icy moon, gently heated from below, is likely to be very many rotation periods, we expect the Rossby number to be small. Thus the dynamics can be expected to be profoundly influenced by the rotation of the moon, as will be clear from the numerical experiments presented herein. To demonstrate the nature of rotational constraints in a deep fluid we will also explore how the nature of the solution changes as the Rossby number is increased and the fluid depth decreases. In an appendix we connect our study to the wider rotating convection literature, placing our study in the context of previous work and (Ra, E) space.

2.1.1 Influence of geometry and rotation

Imagine that warming from below associated with a sustained buoyancy flux of magnitude B drives convection into water of depth H as illustrated schematically in Fig. 1. A layer of 3-D, buoyancy-driven turbulence will deepen as the plumes that make it up evolve in time, penetrating into the fluid above. Ultimately the convection will extend over the entire depth H. We now briefly review the scales which naturally emerge.

1. Evolution over time.
   Let us suppose that in the initial stages, plumes extending into the convective layer are so small in scale that they cannot feel the finite depth H. Furthermore for times $t << f^{-1}$ (where $f = 2\Omega$), rotation is unimportant; only B remains as the controlling parameter. It is then not possible to construct scales for the depth, buoyancy, or velocity of the plumes. The convective process must evolve in time, and we suppose that it proceeds in a self-similar way. The following scales can be formed from B (units of velocity times acceleration) and t (a more detailed account can be found in Jones and Marshall (1993) and Maxworthy and Narimousa (1994)):
   $$l \ \sim \left(Bt^3\right)^{1/2}; u \ \sim (Bt)^{1/2}; g' \ \sim \left(\frac{B}{t}\right)^{1/2} \tag{2}$$
   where l is a measure of the length scale of the convective motion, u is a velocity scale and g' is a measure of the reduced gravity (equivalently buoyancy) of the convective elements.
2. Scale constrained by ocean depth.
   If it is the depth H that ultimately limits the scale of the cells then putting $l = H$ in eq. (2), above, the following scaling is suggested (Deardorff, 1980), independent of rotation:
   $$l \ \sim l_{\mathrm{norot}} = H; u \sim \ u_{\mathrm{norot}} = (BH)^{1/3}; g' \sim \ g'_{\mathrm{norot}} = \left(\frac{B^2}{H}\right)^{1/3} \tag{3}$$
   The subscript "norot" indicates that these are the scales adopted in the absence of rotation.
3. Scale constrained by rotation.
   If H is sufficiently large then the evolving convection will come under rotational control before it reaches the surface. The transition from 3-D buoyancy-driven plumes to quasi-2-D, rotationally dominated motions will occur as t approaches f^{-1}, at which point, replacing t by f^{-1} in eq. (2), the following scales pertain (Fernando et al., 1991):
   $$l \ \sim l_{\mathrm{rot}} = \left(\frac{B}{f^3}\right)^{1/2}; u \ \sim u_{\mathrm{rot}} = \left(\frac{B}{f}\right)^{1/2}; g' \ \sim g'_{\mathrm{rot}} = (Bf)^{1/2} \tag{4}$$
   where the subscript "rot" (for "rotation") has been used to denote the scales at which rotation begins to be important.
   As the plumes keep supplying warm water upwards, they eventually coalesce to form a columnar structure stretching from the bottom all the way to the top. If the column has a buoyancy anomaly set by the entraining, rotationally-constrained plumes given by g'_{rot}, then there is a scale – which we can call a 'deformation' scale – given by
   $$l_{\mathrm{def}} \sim \frac{\sqrt{g'_{\mathrm{rot}} H}}{f} = (l_{\mathrm{rot}} H)^{1/2}. \tag{5}$$

It should be noted that the foregoing scales are independent of assumptions concerning eddy viscosity and diffusivity provided that they are sufficiently small; they are the velocity, space, and buoyancy scales that can be constructed from the "external" parameters B, f, and H. However the constants of proportionality in equations (3) and (4) will be dependent on viscous/diffusive processes and can be determined experimentally from laboratory and numerical experiments. Below we will present numerical experiments which test and provide broad support for these scaling ideas in the context of icy moons.

2.2 Key non-dimensional numbers

It is important to identify key non-dimensional numbers that govern the problem because more often than not, it is not possible to carry out numerical experiments in realistic parameter regimes. However, by extrapolation, we can infer likely behavior of the real system if parameters are appropriately set. Here we focus on key parameters that characterise the influence of rotation on the convective motion, and the geometry of the spherical shell in which it is occurring.

2.2.1 The Natural Rossby number

The natural Rossby number (Jones & Marshall, 1993; Maxworthy & Narimousa, 1994) compares the scale l_{rot} at which convection comes under the influence of the Earth's rotation, to the total depth of the convective layer H

$$Ro^* = \frac{l_{rot}}{H} = \left(\frac{B}{f^3 H^2}\right)^{1/2} \tag{6}$$

As discussed in Appendix B, Ro^* is proportional to a modified flux Rayleigh number. The scaling for rotating and non-rotating convection set out above can be expressed entirely in terms of Ro^* thus:

$$\frac{u_{\text{norot}}}{fH} = Ro^{*\,2/3} \tag{7}$$

$$\frac{g'_{\text{norot}}}{f^2 H} = Ro^{*\,4/3}, \tag{8}$$

and

$$\frac{u_{\text{rot}}}{fH} = Ro^*, \tag{9}$$

$$\frac{g'_{\text{rot}}}{f^2 H} = Ro^* \tag{10}$$

The scale in eq. (5) can be written:

$$\frac{l_{\text{def}}}{H} = \sqrt{Ro^*}. \tag{11}$$

We will test these scaling laws in our simulations of icy moons presented in Section 4 below.

2.2.2 Deep oceans and the geometry of the tangent cylinder: aspect ratio $\eta = R/(R+H)$

The scaling ideas reviewed above are applied here to convection in a rotating spherical shell. When $Ro^* << 1$, Taylor columns align parallel to the rotation axis. In this limit, the convective dynamics behave differently inside and outside the tangent cylinder — a cylinder whose edges are parallel to the moon's axis of rotation and are tangential (hence the name) to the ocean's floor at the equator (fig.1). Upright convection takes place inside the tangent cylinder, whereas roll-like convection takes place outside it. The latitude at which the tangent cylinder intersects the surface depends on the depth of the ocean (the difference between the outer and inner radii, r_o and r_i, respectively). The ratio of these two radii, $\eta = R/(R+H)$, therefore, is the other key non-dimensional number that determines the dynamics and heat transport properties, in addition to Ro^*.

2.2.3 Typical non-dimensional numbers for icy moons

Without running any experiments, the two aforementioned non-dimensional numbers, Ro^* and η, can inform us about the likely dynamics on icy moons. Key physical parameters and derived non-dimensional numbers for four major icy satellites, Enceladus, Titan, Europa, and Ganymede, are summarised in Table 1. The natural Rossby number Ro^* for all is smaller than 2×10^{-4}, indicating that tens of thousands of rotation periods would have passed before a buoyant water parcel rising from the bottom makes it to the surface. Thus we expect ocean dynamics to be governed by rotation. The ratios of inner to outer radii η on icy moons are thought to be around 0.8-0.9, providing ample opportunity for the heat to be redistributed in three dimensions around the globe. In the remainder of our paper, we will perform an array of ultra-high resolution numerical experiments to explore the two dimensional parameter space of Ro^* and η to fill in the detailed dynamics.

3 Configuration of an idealised model for the study of icy moons heated from below

We adopt a highly idealised equation of state for a fresh ocean, in which the density depends only on temperature with a coefficient of thermal expansion, $\alpha = 1.67 \times 10^{-4}\,\mathrm{K}^{-1}$. At the upper boundary we relax the temperature to $0\,\mathrm{K}$. The circulation is energised from below by imposing a spatially-uniform heat flux at the bottom of the ocean. This should be contrasted with the classic (Rayleigh) convection problem in which a temperature contrast is imposed across the fluid. Here the bulk vertical temperature is not externally set but becomes part of the solution. Because the boundary conditions are homogeneous in space, any emergent structures and spatial scales must be a consequence of rotational, geometrical (spherical shell), and fluid-dynamical effects.

We consider a simplified problem in which we solve equations governing the evolution of a fluid on a deep spherical shell allowing for the representation of both horizontal and vertical components of rotation. The equations solved are described in detail in Appendix A, and encode the deep beta-plane equations written down in Dellar (2011) which have their roots in theoretical work by Grimshaw (1975). Use of this approximate set of equations permits the adoption of a Cartesian grid yet captures key spherical effects including a full treatment of the Coriolis acceleration and relaxing the deep atmosphere approximation. A regular horizontal grid facilitates the use of very efficient numerical methods that are well-suited to GPU architectures thus rapidly accelerating compute times. This enables us to carry out many experiments at reasonable clock-time. The rotation rate is set to $5.30\times10^{-5}\,\mathrm{s}^{-1}$, a constant acceleration due to gravity of $0.1\,\mathrm{m\,s}^{-2}$ is assumed, both chosen to represent those on Enceladus. The open-source model we have developed is known as Oceananigans and is coded in Julia, as described in Ramadhan et al (2021).

Table 1. Physical parameters and key non-dimensional numbers for icy moons (Soderlund, 2019), compared to atmospheric and oceanic convection on Earth (Marshall & Schott, 1999).

	Enceladus	Titan	Europa	Ganymede	Earth atmos.	Earth ocean
g $(\mathrm{m\,s^{-1}})$	0.1	1.4	1.3	1.4	10	10
$\Omega\,(10^{-6}\,\mathrm{s^{-1}})$	53	4.6	21	10	7.3	7.3
$Q\,(\mathrm{mW\,m^{-2}})$	80	20	100	40	2×10^5	2×10^5
$\rho\,(10^3\mathrm{kg\,m^{-3}})$	1	1.2	1.1	1.2	10^{-3}	1
$C_\mathrm{p}\,(10^3\mathrm{J\,kg^{-1}\,K^{-1}})$	4	3	3.8	3	4	4
$\alpha\,(10^{-4}\mathrm{K^{-1}})$	0.1	3	2	2.5	30	2
$B\,(10^{-12}\ \mathrm{m^2 s^{-3}})$	0.02	2.3	6.4	3.9	6×10^9	1×10^5
$H\,(\mathrm{km})$	40	300	120	300	10	4
$R\,(\mathrm{km})$	252	2575	1561	2631	6400	6400
η	0.84	0.88	0.92	0.89	0.9984	0.9993
$Ro^*(\times10^{-6})$	3.2	180	77	73	4.4×10^6	4.5×10^4

A representative solution is shown in Fig. 2 for the case when $Ro^* << 1$ and η is small. As expected we obtain a highly structured solution in which the flow is aligned with the axis of the moon's rotation. We observe water at the bottom of the ocean warming up and rising in the water column, not in the direction of gravity, but rather in the direction of the rotation vector. Meanwhile the zonal current (into the page) changes little in the direction of Ω, a manifestation of the Taylor-Proudman theorem.

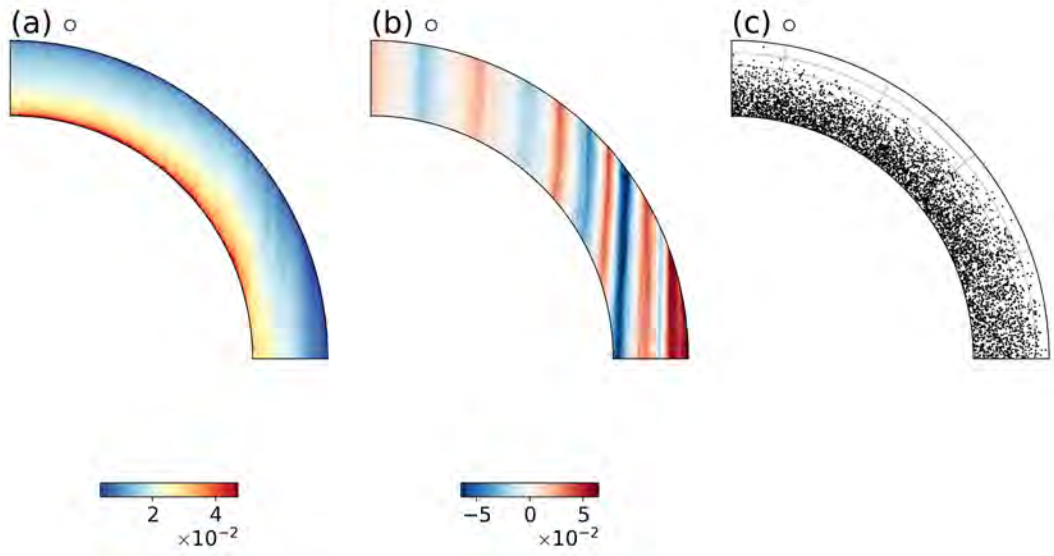

Figure 2. Sections of instantaneous (a) temperature, (b) zonal velocity, and (c) instantaneous location of particles showing the alignment of convection with the local rotation vector in a deep spherical shell governed by deep beta-plane dynamics. The model extends from -90° to 90°N, and simulates a domain of width 50 km. Only the northern hemisphere is shown in this figure for clarity. The parameters and non-dimensional numbers of this experiment are given in Table 2, row ○.

We carry out the suite of experiments summarised in table 2, in which depths, heat fluxes, and rotation rates are varied. These are set out in graphical form as a function of Ro^* and η in Fig. 3. For reference the position of Enceladus and Europa in this phase space is also marked. All experiments are integrated out to steady state. Note from table 2 and fig. 3 we also carry out two experiments with a rotation rate which is 10 times slower than our reference, thus enabling us to explore much higher (Ro^*) regimes approaching that of convection in Earth's atmosphere and ocean. Additionally, three experiments with smallest η are replicated with a viscosity that is two orders of magnitude higher. They are not shown in fig. 3 because they occupy the same locations as the experiments with lower viscosity. The Prandtl number (ratio of viscosity to diffusivity) for all experiments is set to be unity.

4 Phenomenology of ocean circulations

In this section, we present our solutions (section 4.1), interpret them in terms of our scaling laws for the intensity and scale of turbulent motions (section 4.2), examine the large-scale temperature and current speeds in terms of a generalized thermal wind relation (section 4.3) and discuss the parameters that control the latitudinal dependence of vertical heat transport at the upper boundary of the model (section 4.4). In the first three parts, we will focus on the first nine experiments from table 2 with low viscosity,

Table 2. A list of the simulations carried out in the study, along with corresponding key non-dimensional numbers – see Appendix for more details. H is the height of the domain, Q is the bottom heat flux, Ω is the rotation rate of the moon, Ro^* is the natural Rossby number, η is the ratio of inner to outer radius, E is the Ekman number, Ra is the Rayleigh number, and Nu is the Nusselt number.

	H (km)	Q ($\mathrm{W\,m^{-2}}$)	Ω ($10^{-5}\,\mathrm{s^{-1}}$)	Ro^* ($\times10^{-5}$)	η	E ($\times10^{-8}$)	Ra ($\times10^{10}$)	Nu ($\times10^{3}$)
$\boxplus$	10	500	5.3	410	0.96	180	1.2	0.23
$\oplus$	10	50000	5.3	4100	0.96	180	6.3	4.4
$\otimes$	10	100000	0.53	1.9×10^{5}	0.96	1800	4.4	13
$+$	30	500	5.3	140	0.88	21	36	0.58
$\dagger$	30	50000	5.3	1400	0.88	21	190	11
$\times$	30	100000	0.53	6.2×10^{4}	0.88	210	140	30
$\circ$	60	10	5.3	9.8	0.76	5.2	47	0.14
$\lhd$	60	500	5.3	69	0.76	5.2	260	1.3
$\rhd$	60	10000	5.3	310	0.76	5.2	800	8.3
$\bullet$	60	10	5.3	9.8	0.76	520	3.5×10^{-3}	1.9×10^{-3}
$\blacktriangleleft$	60	500	5.3	69	0.76	520	1.9×10^{-2}	1.8×10^{-2}
$\blacktriangleright$	60	10000	5.3	310	0.76	520	8.7×10^{-2}	7.6×10^{-2}

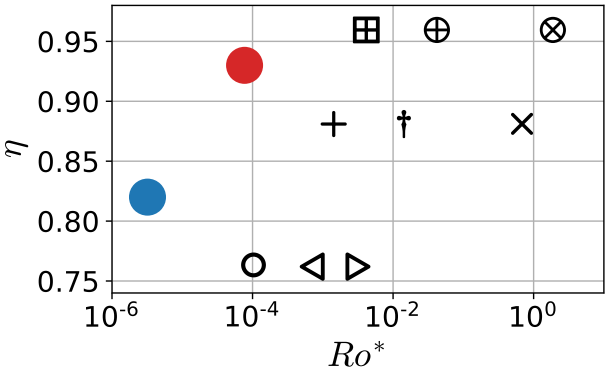

Figure 3. The position in (Ro^*,η) phase space of nine key experiments which span the phase space of the complete set of experiments set out in Table 2. The positions of Enceladus and Europa in this phase space are marked by blue and red circles, respectively.

as inclusion of the three experiments with higher viscosity does not change the results. The three experiments with higher viscosity are discussed in section 4.4, where they help us explore the behavior of meridional heat transport in a wider range of parameter space.

4.1 Convectively-driven turbulence in the spherical shell

Table 3. The means $(\bar{\cdot})$ and standard deviations $(\hat{\cdot})$ of vertical velocity, zonal velocity, and temperature for various experiments are shown in this table. fig. 4 shows $(w_{\mathrm{xy}} - \bar{w}_{\mathrm{xy}})/\hat{w}_{\mathrm{xy}}$, fig. 5 shows $(w_{\mathrm{yz}} - \bar{w}_{\mathrm{yz}})/\hat{w}_{\mathrm{yz}}$, fig. 6 shows $(u - \bar{u})/\hat{u}$, fig. 8 shows $(T - \bar{T})/\hat{T}$.

	$\bar{w}_{\mathrm{xy}}$ ($10^{-9}\,\mathrm{mm\,s^{-1}}$)	$\hat{w}_{\mathrm{xy}}$ ($\mathrm{mm\,s^{-1}}$)	$\bar{w}_{\mathrm{yz}}$ ($\mathrm{mm\,s^{-1}}$)	$\hat{w}_{\mathrm{yz}}$ ($\mathrm{mm\,s^{-1}}$)	$\bar{u}$ ($\mathrm{mm\,s^{-1}}$)	$\hat{u}$ ($\mathrm{mm\,s^{-1}}$)	$\bar{T}$ (K)	$\hat{T}$ (K)
$\boxplus$	-0.27	14.5	-0.28	13.5	-3.86	90.7	1.16	0.07
$\oplus$	20.2	71.7	1.92	64.6	-51.6	364	36.5	0.53
$\otimes$	204	120	4.5	99.4	-42.4	195	50.9	0.45
$+$	2.12	15.8	0.675	14.3	12.5	137	0.56	0.06
$\dagger$	-59.5	90	4.65	83.8	-32.7	298	10.6	0.42
$\times$	0	145	17.2	129	-723	467	25.1	0.54
$\circ$	-2.78	3.47	0.237	3.07	1.62	22.1	0.02	0.01
$\lhd$	-6.37	18.5	3.37	16.5	3.2	123	0.23	0.05
$\rhd$	68	55.1	3.84	49.5	-5.92	258	1.32	0.20

Figures 4 (plan view) and 5 (meridonal section) present snapshots of the vertical velocity from nine solutions spanning (Ro^*, η) space chosen to highlight the nature of the solutions and how they change with Ro^* and η. All plots are shown after the solutions have reached statistical equilibrium. Black lines on the plan views mark where the tangent cylinder cuts through the mid-depth horizontal surface and, in the meridional sections, mark the positions of the tangent cylinder. On moving from left to right Ro^* increases from small (order 10^{-4}) to large (order 1), and on moving in rows upwards, η increases from 0.76 to 0.96. For small Ro^* it is clear that rotational constraints are very strong with the fluid being arranged in columns parallel to Ω. This is most clearly evident in the bottom left solution from each figure, the one from which Fig.2 is taken. Outside of the tangent cylinder (equatorward of the back lines) we see w organised into rolls, whereas inside of the tangent cylinder (poleward of the black lines) the convection is more granular and plumy. For large Ro^* no such rotational constraint is felt and the convection is sensitive to the direction of gravity rather than that of Ω).

In the fast rotating regime (marked by a small natural Rossby number), and in accord with the Taylor-Proudman theorem, flows tend not to vary along the axis of rotation, as is very clear from Fig.2. This is also evident in Fig.4g, 5g and 6g which show instantaneous w (in plan and meridional section) and u (in meridional section) fields, respectively, from the same solution. The differences in dynamics inside and outside the tangent cylinder arise from the differing orientation of the rotation axis with respect to that of gravity. Near the equator, the rotation axis, and therefore the direction of the Taylor columns, is almost parallel to the lower boundary. Swirling motion in planes normal to Ω sweep fluid up and down in almost vertical planes. The rolls form through Rossby wave mode growth supported by the equivalent "beta" effect due to the gradual shortening of Taylor columns away from the rotating axis (Cardin & Olson, 1994; Dormy et al., 2004). With warm water rising and cold water sinking, these equatorial rolls transport heat upward, as shown in the equatorial cross section (figure 7). In high latitudes, the plumes take over, shooting upward along the direction of the rotation axis while spinning around it. During the spin-up, particles released into the flow at the lower boundary are transported upward more rapidly via the rolls than via plumy convection further poleward, as can be seen in Fig.2, panel c. However, eventually, since tracers/heat are mostly transported along the rotation axis, the heat flux reaching the surface is stronger over the poles (section 4.4) than the equator.

In summary, when Ro^* and η are both small (figs. 4, 5 and fig. 6, lower left), one can vividly see the impact of the tangent cylinder on the motion, dividing the icy moon into two parts comprising very different dynamics. The low latitude regions outside the tangent cylinders are filled by meridionally-aligned columnar rolls which extend out to the latitudes where the tangent cylinder strikes the surface. The smaller is η, the further away from the equator is this latitude (fig. 1) and a greater fraction of the transport properties of the fluid are dominated by rolls.

As we move to the top right of figs. 4, 5 and 6, the effect of rotation is much reduced. With little effect of rotation on the solution, the direction of g rather than Ω dominates (panel c). This transition will be evident in the scaling results we now discuss.

4.2 Intensity and scales of turbulent motion

We now infer the temperature, velocity, and length scales of the turbulence from our numerical simulations and compare them to the scaling laws outlined in section 2.2.1. The temperature and velocity scales in the simulations are defined as:

$$T'_{\text{model}} = \sqrt{\overline{T'^2}}, \tag{12}$$

$$u'_{\text{model}} = \sqrt{\overline{u'^2 + v'^2}}, \tag{13}$$

where $u' = u - \bar{u}$, $v' = v - \bar{v}$, $T' = T - \bar{T}$ and $\bar{(\cdot)}$ denotes a horizontal and time average taken over the entire zonal width and 10 days, respectively. The black markers in figure 9a, b,and c were obtained between $y = 10\,\text{km}$ and $y = 50\,\text{km}$ typical of the equatorial region outside the tangent cylinder, while the red markers were obtained for $y = 200\,\text{km}$ to $y = 300\,\text{km}$ indicative of the polar regions inside the tangent cyclinder. A vertical average was also taken in order to collapse the data to a single point.

In figure 9a and b, the diagnosed horizontal and vertical velocity scales, respectively, are compared against the equations (7) and (9). In panel c, the temperature scales are compared against the equations (8) and (10). To enable comparison with scaling, predicted slopes are indicated by the orange (non-rotating) and blue (rotating) straight lines. We see data points from our model simulations cluster around these lines: for $Ro^* < 0.01$ the points follow rotational scaling, while for $Ro^* > 0.01$ the non-rotational scaling is more relevant.

To ascertain the spatial scales of the rolls, we plotted zonal wavenumber spectrums of mid-depth zonal velocity for all experiments and chose the most dominant wavenumbers. The wavelengths associated with these wavenumbers were scaled by the depth of the ocean and plotted against Ro^* in figure 9d. We again see that for $Ro^* < 0.01$, the zonal length scales of the rolls are in agreement with l_{def} from (11) emphasizing the importance of rotational dynamics.

This scaling analysis indicates that as Ro^* increases the plumes become more radially aligned, thus breaking the geostrophic constraint. This transition from geostrophic circulation to more non-linear circulation has important implications for heat transfer across the ocean and is discussed in more detail in the section 4.4.

4.3 Thermal wind: zonal flow and meridional temperature distribution

The mean meridional gradients in temperature are linked to the mean zonal velocity by the thermal wind relationship, obtained by eliminating the pressure from the meridional and vertical momentum equations, eqs. (A2) and (A3) in Appendix A:

$$f\frac{\partial u}{\partial z} + \frac{\partial(\widetilde{f}u)}{\partial y} = -\frac{\partial b}{\partial y}, \tag{14}$$

where f, $\widetilde{f}$ are the vertical and horizontal components of the Coriolis parameter (defined in eq. (A5) in Appendix A) and b is the buoyancy, here proportional to temperature because there is no salinity. Note the contribution from the horizontal component of the Coriolis parameter which dominates outside the tangent cylinder.

In order to determine the degree of compliance with the thermal wind relationship, we integrate the above in y to get a diagnostic relation for b_{TW}, the buoyancy field which is in thermal wind balance with the zonal velocity field:

$$b_{\mathrm{TW}} = -\int \left[f\frac{\partial u}{\partial z} + \frac{\partial(\widetilde{f}u)}{\partial y} \right] \mathrm{d}y + C. \tag{15}$$

The vertical (radial) profile of buoyancy at the equator is used as the constant of integration C. We correlate the simulated value of b with the diagnosed value, b_{TW}, for all of our simulations and plot the correlation coefficients as a function of natural Rossby number. Experiments with low natural Rossby number are in compliance with thermal wind relationship, except near the top and bottom boundaries, where friction becomes important. The compliance gets progressively weaker with increasing natural Rossby number. Since the natural Rossby numbers on Europa and Enceladus are low, we believe thermal wind balance should be satisfied. In such a scenario, the structure of zonal flow and temperature as predicted by our models, that is, eastward flow at the upper surface outside the tangent cylinder, is likely to be seen on Europa and Enceladus. This is in marked contrast to Soderlund et al. (2013), who predicted westerlies at the equator owing to the very high Rossby number in their simulation (more representative of panel f in fig. 6).

4.4 Latitudinal dependence of vertical heat transport

We now consider how vertical heat transport, uniform at the bottom, varies with latitude at the upper surface. This is of particular interest because the amount of heat being delivered to the ice shell by the ocean has a tendency to induce freezing/melting and be reflected in the ice-shell thickness which may be observable. In our model setup, the bottom heat flux is spatially uniform. However by the time it is transported to the upper boundary it has been redistributed by ocean dynamics and exhibits latitudinal dependence. We expect the transition from the "equatorial rolls" to "polar plumes" across the tangent cylinder (see section 4.1) to be reflected in the heat transport.

To examine this transition, and in the spirit of Amit et al. (2020), we plot the ratio

$$q^{\mathrm{h/l}} = \frac{q^{\mathrm{h}} - q^{\mathrm{l}}}{q^{\mathrm{h}} + q^{\mathrm{l}}} \tag{16}$$

against our key non-dimensional number Ro^* (figure 11a). Here

$$q^{\mathrm{l}} = \frac{\int_{-y^{\mathrm{tc}}}^{y^{\mathrm{tc}}} \int q \,\mathrm{d}x\,\mathrm{d}y}{\int_{-y^{\mathrm{tc}}}^{y^{\mathrm{tc}}} \mathrm{d}x\,\mathrm{d}y}, \tag{17}$$

$$q^{\mathrm{h}} = \frac{\int_{y^{\mathrm{tc}}}^{y^{\mathrm{N}}} \int q \,\mathrm{d}x\,\mathrm{d}y}{\int_{y^{\mathrm{tc}}}^{y^{\mathrm{N}}} \mathrm{d}x\,\mathrm{d}y} + \frac{\int_{-y^{\mathrm{N}}}^{-y^{\mathrm{tc}}} \int q \,\mathrm{d}x\,\mathrm{d}y}{\int_{-y^{\mathrm{N}}}^{-y^{\mathrm{tc}}} \mathrm{d}x\,\mathrm{d}y}, \tag{18}$$

are the spatially-averaged heat fluxes inside and outside the tangent cylinder: q is the heat flux in $W\,\mathrm{m}^{-2}$ at the upper boundary, y^{tc} is the meridional coordinate at which the tangent cylinder intersects the upper surface, and y^{N} is the coordinate of the northern boundary of the domain. Positive or negative values of $q^{\mathrm{h/l}}$ indicate polar or equatorial cooling, respectively.

4.4.1 Dependence on the natural Rossby number

Our nine key experiments show polar cooling at low natural Rossby numbers with a change to uniform cooling at high Rossby numbers (see figure 11a). This is similar to, but somewhat different than Amit et al. (2020). They observe that on increasing the local Rossby number Ro_{loc} or, almost equivalently the ratio of Rayleigh number to transitional Rayleigh number Ra/Ra_T – see Appendix B where non-dimensional numbers are defined and discussed – there is a regime transition from equatorial cooling to polar cooling and finally to uniform cooling. Repeating our three low η experiments but using a higher viscosity, we are able to capture an equatorial cooling regime when using the lowest heat flux. Together, our results show a similar regime transition as that found by Amit et al. (2020). As shown in figure 11b and c, at low Ro_{loc} and Ra/Ra_T, the moons tend to lose heat at lower latitudes, at very high Ro_{loc} and Ra/Ra_T heat loss is spatially uniform and, in between, there is an intermediate regime with polar cooling.

The natural Rossby number largely captures the pattern of polar cooling and also its plateauing to uniform cooling (figure 11a), but fails to differentiate between the two lowest Rossby number cases (○ and •). This happens because increasing viscosity can suppress polar plumes completely, particularly when the bottom heat flux is low (fig. 12a, fig. 14). The direction of the meridional heat transport can reverse with increasing viscosity, as shown in fig. 14. It is clear then that, despite the utility of the natural Rossby number, it cannot provide information about the criticality of the convective system. If plumes are suppressed by viscosity, rolls dominate vertical heat transport resulting in equatorial cooling (e.g. •). Since Ro_{loc} and Ra/Ra_{T} depend on viscosity, they are able to distinguish between high and low viscosity cases.

Although the general $q^{\mathrm{h/l}}$ pattern is broadly similar to Amit et al. (2020), the transition from equatorial cooling to polar cooling occurs at values of Ro_{loc} and Ra/Ra_{T} that are one order of magnitude smaller than those suggested by Amit et al. (2020). It is for this reason that the transitional criteria proposed by Amit et al. (2020) ($Ro_{\mathrm{loc}} = 5.6$ and $Ra/Ra_T = 1$, shown by gray and black dashed lines in fig. 13) fails to differentiate between equatorial and polar cooling cases (shown by circles in fig. 13) – three polar cooling cases fall into the equatorial cooling regime proposed by Amit et al. (2020).

4.4.2 Effect of η

The ratio of inner to outer radius, η, can also affect heat loss patterns (figure 11d). As η approaches unity (shallow ocean), the surface heat flux becomes almost uniform irrespective of the natural Rossby number (e.g. experiments $\times$, $\otimes$). As η decreases (deep ocean), the heat loss patterns tend to undergo equatorial or polar cooling depending on the magnitude of heat flux and viscosity. This pattern arises because at high η the oceans are very shallow which makes it easy for heat to transit across the water column in relatively short time without much meridional transport. On the other hand the excess depth of the oceans at low η facilitates meridional transport of heat. The overall picture that emerges from our experiments is that the rotational regime, characterized by low Rossby number, can exhibit both polar and equatorial cooling. The experiments that resolve plumes tend to support polar cooling. In experiments in which plumes are suppressed, say due to high viscosity, equatorial rolls are more efficient in transporting heat. We imagine that the boundary between polar and equatorial cooling might be blurry and depend upon the Ekman number. This indicates that the role of unresolved turbulence cannot be ignored in establishing the meridional pattern of cooling.

Despite all the above caveats, we cannot resist but to speculate on the implications of our results for icy moons. Europa has ($Ro^* \sim 10^{-4}$ and $\eta \sim 0.93$), and Enceladus has ($Ro^* \sim 10^{-6}$ and $\eta \sim 0.83$) (B1). With such low natural Rossby numbers both are expected to be in the rotation dominant regime, and thus $q^{\mathrm{h/l}}$ will deviate from one. Because of its large η, Europa's ocean may lose heat almost uniformly over the globe. Enceladus has a deeper ocean with respect to its size, and so is likely to have more meridional heat transport. Whether equatorial cooling or polar cooling will dominate will depend on the eddy viscosity/diffusivity in the Enceladean ocean. Previous studies tend to use molecular values of viscosity and diffusivity to locate natural icy moons in Rayleigh-Ekman space. However, according to Rekier et al. (2019), libration motions can generate much turbulence, significantly elevating the viscosities and diffusivities above molecular values. According to the estimate in Kang et al. (2021), the turbulent viscosity in Enceladus' ocean might be as high as $O(10^{-3}\,\mathrm{m^2\,s^{-1}})$. Assuming this viscosity, we estimate the $RaE^{4/3}$ and E for Enceladus and mark these values with a grey diamond in fig. 13. Limited by computational resources, we cannot integrate an experiment out to equilibrium with a realistic heat flux (3 orders magnitude smaller than the lowest heat flux employed here), and we do not yet have enough experiments to identify a universal scaling law. It remains unclear to us, therefore, what form the meridional profile of heat loss will take on a hypothetical Enceladus heated only from below.

5 Summary and discussion

We have explored and attempted to rationalise the ocean dynamics and heat transport on icy moons using a novel set of high-resolution large eddy simulations. Departing from previous studies (Soderlund et al., 2013; Soderlund, 2019; Amit et al., 2020), we have attempted to organise our experiments in terms of the natural Rossby number, Ro^*, and the ocean's aspect ratio η. Importantly, rather than preseribe a temperarure difference across the fluid, at the bottom we have prescribed a heat flux. Moreover, we have reduced the heat flux as much as possible (the lowest heat flux used here is $10\,\mathrm{W\,m^{-2}}$). This increases the computational cost, but is somewhat offset by the new-generation GPU-based modelling technique employed. As a result, we have attempted to get closer to a realistic regime than in previous studies. Finally we have reduced the diffusivity and viscosity to levels that may be close to the mixing induced by the libration motions on Enceladus (Rekier et al., 2019).

Our main findings are listed below:

1. All simulations, except those with unrealistically large heat fluxes and hence high Rossby numbers, display two regions of circulation demarcated by the tangent cylinder. Inside the tangent cylinder (high latitudes), rotationally-modified convective "plumes" dominate; they shoot upward parallel to the rotation axis. Outside the tangent cylinder (low latitudes), "rolls" dominate; they swirl in the equatorial plane about the direction of rotation.
2. An appropriately defined Rossby radius of deformation determines both the horizontal scales of the polar plumes and the zonal scales of the equatorial rolls. The horizonal and vertical velocities scale with u_{rot} and u_{norot} in, respectively, low and high Ro^* regimes.
3. Thermal wind balance is generally satisfied at low Rossby numbers, and is violated when rotational effects become negligible at $Ro^* > 0.1$.
4. The efficiency of vertical heat transport varies with latitude because of the different dynamics inside and outside the tangent cylinder. Whether heat will be lost more to the equatorial ice shell or the polar ice shell cannot be convincingly predicted by the diffusivity/viscosity-independent natural Rossby number, despite its prediction power regarding the roll/plume dynamics. This is because increasing diffusivity/viscosity may selectively switch off the plume dynamics. We also examined the non-dimensional numbers Ro_{loc} and Ra/Ra_{T}, which have been proposed to correlate with the relative heat transport efficiency in low and high latitudes (Amit et al., 2020). Neither Ro_{loc} or Ra/Ra_{T} simultaneously fit our results and those of Amit et al. (2020).
5. The relative heat transport efficiency of low vs high latitudes depends not only on the fluid dynamical non-dimensional numbers, such as Rossby number (or Rayleigh number) and Ekman number, but also on the aspect ratio of the ocean η. When the ocean is shallow, the heat flux at the water-ice interface remains very similar to the heat flux imposed at the bottom. In contrast, when the ocean is deep, meridional transport of heat occurs depending on the relative efficiency of plumes and rolls in heat transport.

The meridional heat redistribution by the ocean can induce freezing and melting to the ice shell and eventually reshape it. The ice shell geometry can be more easily measured than subsurface properties and therefore understanding how meridional heat redistribution occurs and on what it depends is highly relevant. Due to the limited number of experiments we can carry out at this state-of-the-art resolution, we cannot yet identify a universal scaling law for heat transport, and this calls for further numerical and theoretical studies.

Appendix A Modeling framework: equations with non-traditional Coriolis in Cartesian coordinates

We adopt a Cartesian framework to motions in spherical geometry that capture the change with latitude of the angle between the rotation vector and gravity. Derivations of such equation sets was pioneered by Grimshaw (1975), who wrote down a non-traditional beta-plane set for flow on a rotating planet in which the vertical component of the Coriolis parameter was allowed to vary in the horizontal, whilst the horizontal component (set to zero on the traditional beta plane) was kept constant. Dellar (2011) significantly advanced Grimshaw's work by using Hamilton's principle to derive a non-traditional set in which both components of Coriolis are allowed to vary in latitude, without sacrificing conservation properties. We employ an equation set inspired by Dellar's work appropriate for a deep fluid where ω and g are not parallel to one-another.

In Cartesian coordinates (x, y, z) with x, pointing eastwards, y pointing northwards and z pointing upwards in the direction opposite to gravity, the equations with non-traditional Coriolis are written thus:

$$\frac{\mathrm{D}u}{\mathrm{D}t} + \widetilde{f}w - fv = -\frac{1}{\rho_{\mathrm{ref}}}\frac{\partial p}{\partial x} + F^{\mathrm{x}}, \tag{A1}$$

$$\frac{\mathrm{D}v}{\mathrm{D}t} + fu = -\frac{1}{\rho_{\mathrm{ref}}}\frac{\partial p}{\partial y} + F^{\mathrm{y}}, \tag{A2}$$

$$\frac{\mathrm{D}w}{\mathrm{D}t} - \widetilde{f}u - b = -\frac{1}{\rho_{\mathrm{ref}}}\frac{\partial p}{\partial z} + F^{\mathrm{z}}, \tag{A3}$$

where $\mathbf{u} = (u, v, w)$ is the velocity, g is acceleration due to gravity assumed to be constant, ρ_{ref} a constant reference density, p is the pressure, $\frac{\mathrm{D}}{\mathrm{D}t} = \frac{\partial}{\partial t} + \mathbf{u}\cdot\nabla$ is the total derivative, and F's on the RHS represent momentum sources and sinks given by

$$(F^{\mathrm{x}}, F^{\mathrm{y}}, F^{\mathrm{z}}) = \nu\nabla^2\mathbf{u}, \tag{A4}$$

where ν is the viscosity. It is set to $2{\times}10^{-2}\,\mathrm{m}^2\,\mathrm{s}^{-1}$ for the first nine experiments in table 2 and elevated to $2\,\mathrm{m}^2\,\mathrm{s}^{-1}$. Additionally, no-slip boundary conditions act as sinks of momentum at the bottom and on the sidewalls.

The Coriolis parameter is

$$\mathbf{f} = (0, f, \widetilde{f}) = 2\Omega(0, \cos y/R, \sin y/R), \tag{A5}$$

where y/R increases from 0 to 1.4 (80°) where $R = 251\,\mathrm{km}$ is the radius of the moon, allowing us to mimic the mis-alignment of the rotation vector and gravity on the sphere but in a Cartesian framework: see the Taylor Columns in Fig.2 even though the simulations were performed on a Cartesian grid.

Along with the momentum equations we have the continuity equation,

$$\nabla\cdot\mathbf{u} = 0. \tag{A6}$$

The buoyancy is related to temperature by a linear equation of state,

$$b = \alpha g(T - T_0), \tag{A7}$$

where T_0 is a reference temperature and α is the thermal expansion coefficient assumed to be constant. Temperature evolves in time according to the equation

$$\frac{\mathrm{D}T}{\mathrm{D}t} = \kappa\nabla^2 T + \delta_{\mathrm{top}}\frac{T - T_0}{\tau} + \frac{\delta_{\mathrm{bottom}}}{\Delta z}\frac{Q}{\rho_{\mathrm{ref}}C_{\mathrm{p}}}, \tag{A8}$$

where, κ is the diffusivity, $\delta_{\mathrm{top}} = 1$ at the topmost grid point and zero elsewhere, $\delta_{\mathrm{bottom}} = 1$ at the bottom grid point and zero elsewhere, Q is the uniform heat flux imposed at the bottom, Δz is the vertical grid spacing, and $C_{\mathrm{p}} = 4000\,\mathrm{J\,kg^{-1}\,K^{-1}}$ is the specific heat constant of water. Diffusivity is set equal to the viscosity. The second term on the RHS relaxes the temperature at the top to T_0 with a relaxation time scale

$$\tau = \frac{\Delta z^2}{20\kappa} = 2x10^6\,\mathrm{s}, \tag{A9}$$

which is about 2.3 Earth days, and represents the loss of heat from the ocean to the ice shell.

The above equations are discretized on a domain $x \subseteq [0, 50]\,\mathrm{km}$, $y \subseteq [-352, 352]\,\mathrm{km}$, and $z \subseteq [-H, 0]$, with $\Delta x = \Delta y = \Delta z = 300\,\mathrm{m}$ and coded up in the framework provided by Oceananigans.jl (Ramadhan et al., 2020), open source software developed for studies of ocean process. Oceananigans is written in the Julia programming language (Bezanson et al., 2017) and runs fast on GPUs enabled by Julia's native GPU compiler (Besard et al., 2019). To solve equations (A1)–(A8) Oceananigans.jl uses a staggered C-grid finite volume spatial discretization (Arakawa & Lamb, 1977) with an upwind-biased 5^{th}-order weighted essentially non-oscillatory (WENO) advection scheme for momentum and tracers (Shu, 2009). Diffusion terms are computed using centered 2^{nd}-order differences. A pressure projection method to ensure the incompressibility of $\mathbf{u}$ at every time step (Brown et al., 2001) is used. A fast Fourier-transform-based eigenfunction expansion of the discrete second-order Poisson operator is used to solve the discrete pressure Poisson equation for the pressure on a regular grid (Schumann & Sweet, 1988). An explicit 3^{rd}-order Runge-Kutta method is used to advance the solution in time (Le & Moin, 1991).

Appendix B Interpretation in terms of Rayleigh number and Ekman number space.

Historically, Rayleigh number Ra and Ekman number E (or equivalently Taylor number Ta),

$$\mathrm{Ra} \equiv \frac{\alpha g \Delta T H^3}{\nu\kappa} \tag{B1}$$

$$\mathrm{Ta} \equiv \frac{1}{E^2} \equiv \left(\frac{2\Omega H^2}{\upsilon}\right)^2, \tag{B2}$$

have often been used to characterize the strength of convective instability and rotation relative to diffusive/viscous processes in the study of convection between two perfectly flat and uniform lids held at different temperatures.

Using this framework, Boubnov and Golitsyn (1990); Gastine et al. (2016); Soderlund et al. (2013); Soderlund (2019) and Amit et al. (2020) employed a diagram that divides the (Ra, E) plane into differing dynamical regimes. As the flux Rayleigh number and Taylor number increases, the convective system goes through (1) the conduction regime in which diffusion suppresses convective instability, (2) a regime of regular overturning in which convection takes the form of uniform cells, (3) a geostrophic turbulence regime and (4) a fully turbulent regime. In regime (1) and (2), the equatorial convective rolls, swirling in the longitude-z plane, are more efficient in vertical heat transport, leading to the equator-amplified heat flux at the top. In the opposite limit (high heat flux and low viscosity/diffusivity), convective plumes shoot radially upwards unaware of planetary rotation, leading to globally-uniform heat delivery to the upper boundary. It appears that in between the two regimes, high-latitude convection can be more efficient than tropical convection in vertical heat transport, but only in a rather limited range of parameter space (Amit et al., 2020).

However, there are two unsatisfactory aspects of the (Ra, E) pairing. As can be seen from Eq.B1-B2, each depends critically on the viscosity and diffusivity, which are likely to be much larger than molecular values due to eddy-induced mixing processes which are poorly constrained, if at all. Regime transitions have been suggested which depend on some combination of (Ra, E), in which the dependence on viscosity and diffusivity largely cancels out leaving scaling results which depend on the external parameters preferred here. Additionally, convection on icy moons is not driven by a prescribed temperature difference between the top and bottom boundaries. Instead, the magnitude of the heat flux is set by the total dissipation rate of the system and the top-to-bottom temperature difference evolves in response. Therefore, a more natural non-dimensional number for our problem is the modified flux Rayleigh number Ra_q^* (Christensen, 2002; Christensen & Aubert, 2006; J. M. Aurnou et al., 2020):

$$\mathrm{Ra}_\mathrm{q}^* \equiv \frac{\alpha g \overline{Q}}{\rho C_p \Omega^3 H^2}. \tag{B3}$$

Importantly, Ra_q^* does not depend on the poorly constrained viscosity and diffusivity, and it uses the more natural bottom heat flux Q to replace the bottom-to-top temperature difference ΔT. In fact, Ra_q^* is proportional to the natural Rossby number of

Jones and Marshall (1993) and Maxworthy and Narimousa (1994) that we have employed in the main body of this paper. Moreover, the scaling laws based on Ra_q^* have been shown to successfully predict the system's Nusselt number and Rossby number (Christensen, 2002; Christensen & Aubert, 2006; J. M. Aurnou et al., 2020). In the asymptotic regime that is approached at sufficiently small Ekman numbers,

$$\mathrm{Ro} \equiv \frac{U}{\Omega L} = 0.65(Ra_\mathrm{q}^*)^{1/5}, \tag{B4}$$
$$\mathrm{Nu}^* \equiv \frac{Q}{\rho C_\mathrm{p}\Delta T \Omega D} = 0.077(Ra_\mathrm{q}^*)^{5/9}. \tag{B5}$$

Here Rossby number Ro characterize the importance of advection and inertia relative to the rotation, and Nusselt number Nu^* characterizes the strength of dynamics compared to diffusion. Our simulations are in accord with these scalings, as can be seen in figure B1, and demonstrating that our simulations have approached the asymptotic scaling. Our constants of proportionality are different from those in previous studies but we attribute them to differences in model setups. We therefore argue that eddy-induced mixing dominates the molecular viscosity/diffusivity and further reduction of the explicit diffusivity/viscosity used in our simulations will not significantly change our results.

Furthermore, Gastine et al. (2016) demarcated the conductive, weakly non-linear, rapidly rotating, transitional, and non-rotating regimes in the Ra, E space. Our experiments lie in the transitional and the non-rotating regimes according to their classification (Fig.13). It should be noted that the natural Rossby number increases as our simulations scan the space from the transitional regime to non-rotating regime indicating that the Rossby number can serve as an excellent metric for judging the importance of rotation in setting the dynamics.

We have also plotted the ratio of polar to equatorial cooling against the local Rossby number, $Ro_\mathrm{loc} = Ra^{5/4}\, E^2$, and ratio of Rayleigh number to transitional Rayleigh number, $Ra/Ra_\mathrm{T} = 0.1\, Ra\, E^{3/2}$, in order to compare our results against those of Amit et al. (2020) in fig. 11b and c. Our results are similar to theirs further confirming that our results do not differ significantly upon interpretation in the Ra, E space.

Acknowledgments

The authors would like to thank the Exploring Ocean Worlds (`https://oceanworlds.whoi.edu/exploring-ocean-worlds/`) project for funding this research and providing regular feedback. WK would like to thank the Lorenz/Houghton fellowship at MIT for supporting her. SB would like to thank Oliver Jahn for help with model setup and analysis. Computational resources for this project were supplied by Svante and Satori clusters at MIT. Please visit `10.5281/zenodo.5228689` to download data used in this study.

References

Amit, H., Choblet, G., Tobie, G., Terra-Nova, F., Čadek, O., & Bouffard, M. (2020, Mar). Cooling patterns in rotating thin spherical shells — Application to Titan's subsurface ocean. *Icarus*, *338*, 113509. Retrieved from `http://dx.doi.org/10.1016/j.icarus.2019.113509` doi: 10.1016/j.icarus.2019.113509

Arakawa, A., & Lamb, V. R. (1977). Computational Design of the Basic Dynamical Processes of the UCLA General Circulation Model. In *Methods in Computational Physics: Advances in Research and Applications* (Vol. 17, pp. 173–265). Elsevier. doi: 10.1016/B978-0-12-460817-7.50009-4

Aurnou, J., Andreadis, S., Zhu, L., & Olson, P. (2003, Jul). Experiments on convection in Earth's core tangent cylinder. *Earth Planet. Sci. Lett.*, *212*(1-2), 119–134. Retrieved from `http://dx.doi.org/10.1016/S0012-821X(03)00237-1` doi: 10.1016/s0012-821x(03)00237-1

Table B1. The non-dimensional numbers estimated for the simulations performed in this study.

	H (km)	Q ($\mathrm{W\,m^{-2}}$)	η	Ro^* $\times 10^{-5}$	Ra $\times 10^{10}$	Ra^* $\times 10^{-4}$	Ra^*_q $\times 10^{-7}$	E $\times 10^{-8}$	Nu^* $\times 10^{-6}$	Nu $\times 10^{3}$	Ro_loc
$\boxplus$	10	500	0.96	410	1.2	390	170	180	420	0.23	13
$\oplus$	10	50000	0.96	4100	6.3	2100	1.7×10^4	180	7900	4.4	100
$\otimes$	10	100000	0.96	1.8×10^5	4.4	14×10^4	3.3×10^7	1800	2.3×10^5	13	6.6×10^3
$+$	30	500	0.88	140	36	160	19	21	120	0.58	12
$\dagger$	30	50000	0.88	1400	190	850	1900	21	2200	11	100
$\times$	30	100000	0.88	6.2×10^4	140	6.2×10^4	3.8×10^6	210	6.2×10^4	30	6.7×10^3
$\circ$	60	10	0.76	9.8	47	13	9.5×10^{-2}	5.2	7.4	0.14	1.1
$\lhd$	60	500	0.76	69	260	71	4.8	5.2	67	1.3	9.1
$\rhd$	60	10000	0.76	310	800	220	95	5.2	430	8.3	37
$\bullet$	60	10	0.76	9.8	3.5×10^{-3}	9.7	9.5×10^{-2}	520	9.8	1.9×10^{-3}	7.5×10^{-2}
$\blacktriangleleft$	60	500	0.76	69	1.9×10^{-2}	52	4.8	520	92	1.8×10^{-2}	0.61
$\blacktriangleright$	60	10000	0.76	310	8.7×10^{-2}	240	95	520	400	7.6×10^{-2}	4.1

Aurnou, J., Heimpel, M., Allen, L., King, E., & Wicht, J. (2008, Jun). Convective heat transfer and the pattern of thermal emission on the gas giants. *Geophys. J. Int.*, *173*(3), 793–801. Retrieved from `http://dx.doi.org/10.1111/j.1365-246X.2008.03764.x` doi: 10.1111/j.1365-246x.2008.03764.x

Aurnou, J. M., Horn, S., & Julien, K. (2020, October). Connections between non-rotating, slowly rotating, and rapidly rotating turbulent convection transport scalings. *Physical Review Research*, *2*(4), 043115.

Besard, T., Foket, C., & De Sutter, B. (2019). Effective Extensible Programming: Unleashing Julia on GPUs. *IEEE Trans. Parallel Distrib. Syst.*, *30*(4), 827–841. doi: 10.1109/TPDS.2018.2872064

Bezanson, J., Edelman, A., Karpinski, S., & Shah, V. B. (2017). Julia: A Fresh Approach to Numerical Computing. *SIAM Rev.*, *59*, 65–98. doi: 10/f9wkpj

Borucki, J. G., Khare, B., & Cruikshank, D. P. (2002, November). A new energy source for organic synthesis in Europa's surface ice. *JOURNAL OF GEOPHYSICAL RESEARCH-ATMOSPHERES*, *107*(E11), 24–1–24–5.

Boubnov, B., & Golitsyn, G. (1990). Temperature and velocity field regimes of convective motions in a rotating plane fluid layer. *J. Fluid Mech.*, *219*, 215–239.

Brown, D. L., Cortez, R., & Minion, M. L. (2001). Accurate Projection Methods for the Incompressible Navier–Stokes Equations. *J. Comput. Phys.*, *168*(2), 464–499. doi: 10/djz53c

Busse, F. H. (1970, Nov). Thermal instabilities in rapidly rotating systems. *J. Fluid Mech.*, *44*(3), 441–460. Retrieved from `http://dx.doi.org/10.1017/S0022112070001921` doi: 10.1017/s0022112070001921

Cardin, P., & Olson, P. (1994, March). Chaotic thermal convection in a rapidly rotating spherical shell: consequences for flow in the outer core. *Physics of the Earth and Planetary Interiors*, *82*(3-4), 235–259.

Christensen, U. R. (2002, Oct). Zonal flow driven by strongly supercritical convection in rotating spherical shells. *J. Fluid Mech.*, *470*, 115–133. Retrieved from `http://dx.doi.org/10.1017/S0022112002002008` doi: 10.1017/s0022112002002008

Christensen, U. R., & Aubert, J. (2006). Scaling properties of convection-driven dynamos in rotating spherical shells and application to planetary magnetic fields. *Geophysical Journal International*, *166*(1), 97–114. doi: 10.1111/j.1365-246x.2006.03009.x

Deardorff, J. W. (1980, Jun). Stratocumulus-capped mixed layers derived from a three-dimensional model. *Bound. Layer Meteorol.*, *18*(4), 495–527. Retrieved from `http://dx.doi.org/10.1007/BF00119502` doi: 10.1007/bf00119502

Dellar, P. J. (2011, Mar). Variations on a beta-plane: derivation of non-traditional beta-plane equations from Hamilton's principle on a sphere. *J. Fluid Mech.*, *674*, 174–195. Retrieved from `http://dx.doi.org/10.1017/S0022112010006464` doi: 10.1017/s0022112010006464

Dormy, E., Soward, A. M., Jones, C. A., Jault, D., & Cardin, P. (2004, Feb). The onset of thermal convection in rotating spherical shells. *J. Fluid Mech.*, *501*, 43–70. Retrieved from `http://dx.doi.org/10.1017/S0022112003007316` doi: 10.1017/s0022112003007316

Fernando, H. J. S., Chen, R.-R., & Boyer, D. L. (1991, Jul). Effects of rotation on convective turbulence. *J. Fluid Mech.*, *228*, 513. Retrieved from `http://dx.doi.org/10.1017/S002211209100280X` doi: 10.1017/s002211209100280x

Gastine, T., Wicht, J., & Aubert, J. (2016, Nov). Scaling regimes in spherical shell rotating convection. *J. Fluid Mech.*, *808*, 690–732. Retrieved from `http://dx.doi.org/10.1017/jfm.2016.659` doi: 10.1017/jfm.2016.659

Grimshaw, R. H. J. (1975, Jan). A note on the -plane approximation. *Tellus*, *27*(4), 351–357. Retrieved from `http://dx.doi.org/10.3402/tellusa.v27i4.9982` doi: 10.3402/tellusa.v27i4.9982

Hand, K., & Chyba, C. (2007, August). Empirical constraints on the salinity of the europan ocean and implications for a thin ice shell. *Icarus*, *189*(2), 424–438.

Jones, H., & Marshall, J. (1993, Jun). Convection with rotation in a neutral ocean: A study of open-ocean deep convection. *J. Phys. Oceanogr.*, *23*(6), 1009–1039. Retrieved from `http://dx.doi.org/10.1175/1520-0485(1993)023<1009:CWRIAN>2.0.CO;2` doi: 10.1175/1520-0485(1993)023<1009:cwrian>2.0.co;2

Kang, W., Mittal, T., Bire, S., Michel, J., & Marshall, J. (2021). How does salinity shape ocean circulation and ice geometry on enceladus and other icy satellites? *arxiv*.

Le, H., & Moin, P. (1991). An improvement of fractional step methods for the incompressible Navier-Stokes equations. *J. Comput. Phys.*, *92*(2), 369–379. doi: 10/bbcbm8

Marshall, J., & Schott, F. (1999, February). Open-ocean convection: Observations, theory, and models. *Rev. Geophys.*, *37*(1), 1-64.

Maxworthy, T., & Narimousa, S. (1994, May). Unsteady, turbulent convection into a homogeneous, rotating fluid, with oceanographic applications. *J. Phys. Oceanogr.*, *24*(5), 865–887. Retrieved from `http://dx.doi.org/10.1175/1520-0485(1994)024<0865:UTCIAH>2.0.CO;2` doi: 10.1175/1520-0485(1994)024<0865:utciah>2.0.co;2

Postberg, F., Kempf, S., Schmidt, J., Brilliantov, N., Beinsen, A., Abel, B., … Srama, R. (2009). Sodium salts in e-ring ice grains from an ocean below the surface of enceladus. *Nature*, *459*(7250), 1098–1101.

Postberg, F., Khawaja, N., Abel, B., Choblet, G., Glein, C. R., Gudipati, M. S., … others (2018). Macromolecular organic compounds from the depths of enceladus. *Nature*, *558*(7711), 564–568.

Ramadhan, A., Wagner, G. L., Hill, C., Campin, J.-M., Churavy, V., Besard, T., … Marshall, J. (2020). Oceananigans.jl: Fast and friendly geophysical fluid dynamics on gpus. *J. Open Source Softw.*, *5*(53), 2018. doi: 10.21105/joss.02018

Rekier, J., Trinh, A., Triana, S., & Dehant, V. (2019). Internal energy dissipation in enceladus's subsurface ocean from tides and libration and the role of inertial waves. *Journal of Geophysical Research: Planets*, *124*(8), 2198–2212.

Schumann, U., & Sweet, R. A. (1988). Fast Fourier transforms for direct solution of poisson's equation with staggered boundary conditions. *J. Comput. Phys.*, *75*, 123–137. doi: 10/fdkvqq

Shu, C.-W. (2009). High Order Weighted Essentially Nonoscillatory Schemes for Convection Dominated Problems. *SIAM Rev.*, *51*, 82–126. doi: 10.1137/070679065

Soderlund, K. M. (2019, August). Ocean Dynamics of Outer Solar System Satellites. *Geophysical Research Letters*, *46*(15), 8700–8710.

Soderlund, K. M., Schmidt, B. E., Wicht, J., & Blankenship, D. D. (2013, Dec). Ocean-driven heating of Europa's icy shell at low latitudes. *Nat. Geosci.*, *7*(1), 16–19. Retrieved from `http://dx.doi.org/10.1038/NGEO2021` doi: 10.1038/ngeo2021

Stoker, C. R., Boston, P. J., Mancinelli, R. L., Segal, W., Khare, B. N., & Sagan, C. (1990, May). Microbial metabolism of tholin. *Icarus*, *85*(1), 241–256.

Takehiro, S.-I. (2008, Oct). Physical interpretation of spiralling-columnar convection in a rapidly rotating annulus with radial propagation properties of rossby waves. *J. Fluid Mech.*, *614*, 67–86. Retrieved from `http://dx.doi.org/10.1017/S0022112008003194` doi: 10.1017/s0022112008003194

Thomas, P., Tajeddine, R., Tiscareno, M., Burns, J., Joseph, J., Loredo, T., … Porco, C. (2016). Enceladus's measured physical libration requires a global subsurface ocean. *Icarus*, *264*, 37–47.

Trumbo, S. K., Brown, M. E., & Hand, K. P. (2019, June). Sodium chloride on the surface of Europa. *Science Advances*, *5*(6), eaaw7123.

Waite, J. H., Combi, M. R., Ip, W.-H., Cravens, T. E., McNutt, R. L., Kasprzak, W., … Tseng, W.-L. (2006, March). Cassini Ion and Neutral Mass Spectrometer: Enceladus Plume Composition and Structure. *Science*, *311*(5766), 1419–1422.

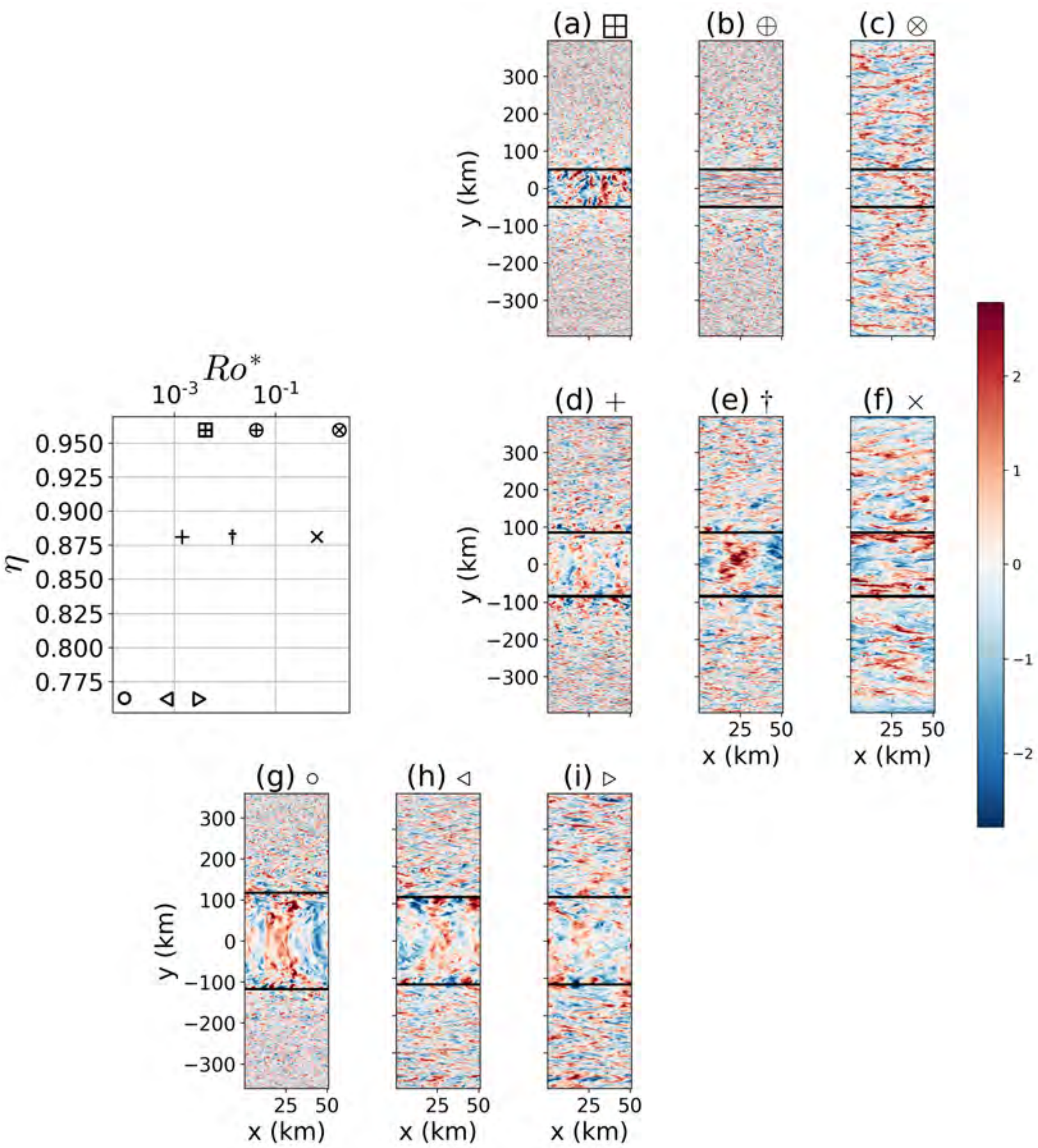

Figure 4. Instantaneous plots of standardised anomalies (see table 3) of vertical velocity at mid-depth are shown for various experiments. The first, second, and third rows represent models with η of 0.96, 0.88, and 0.76, respectively. The natural Rossby number increases towards the right for each row. The latitude at which the tangent cylinder strikes the free surface is shown by the horizontal black line.

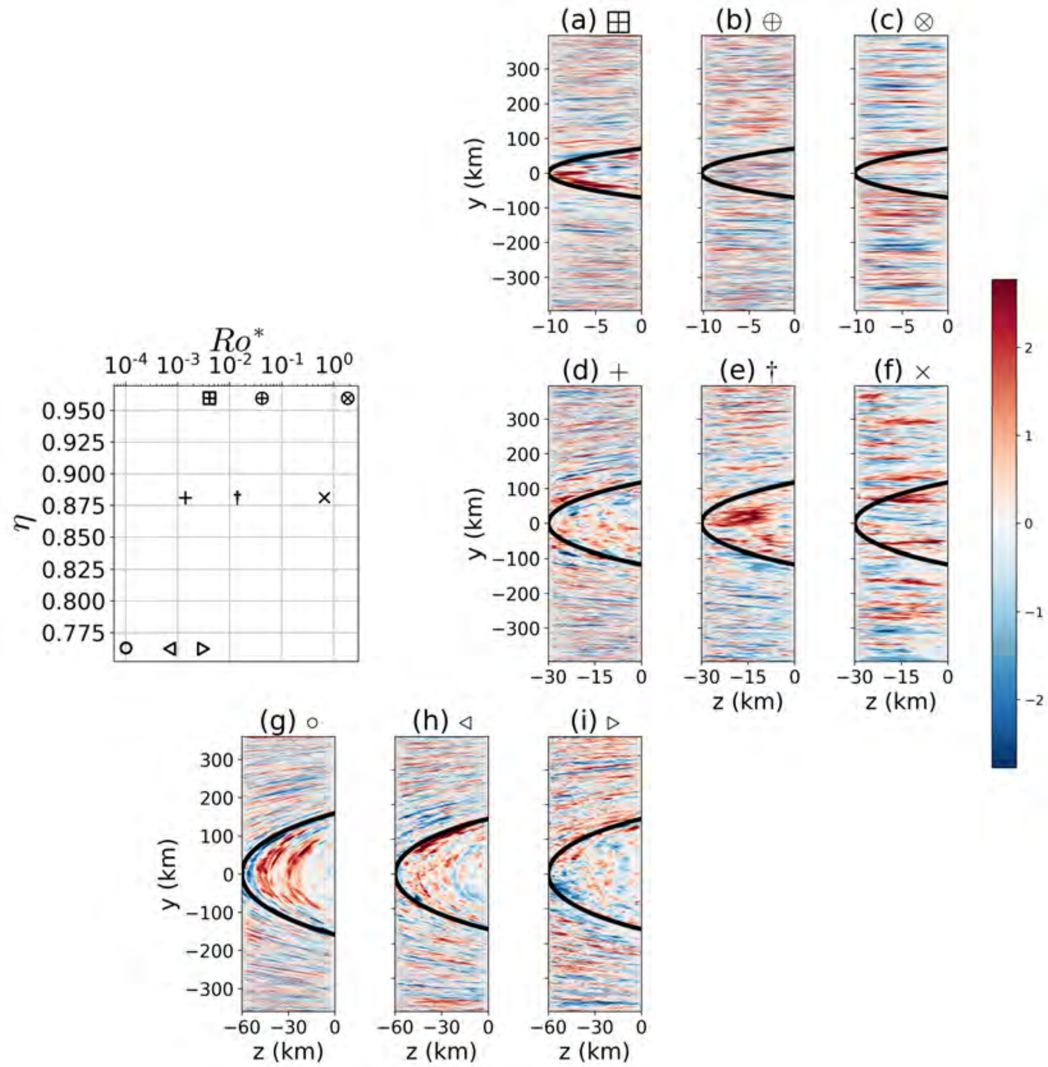

Figure 5. Instantaneous plots of standardised anomalies (see table 3) of vertical velocity at $x = 25\,\mathrm{km}$ are shown for various experiments. The first, second, and third rows represent models with η of 0.96, 0.88, and 0.76, respectively. The natural Rossby number increases towards the right for each row. The tangent cylinder is shown by the horizontal black line.

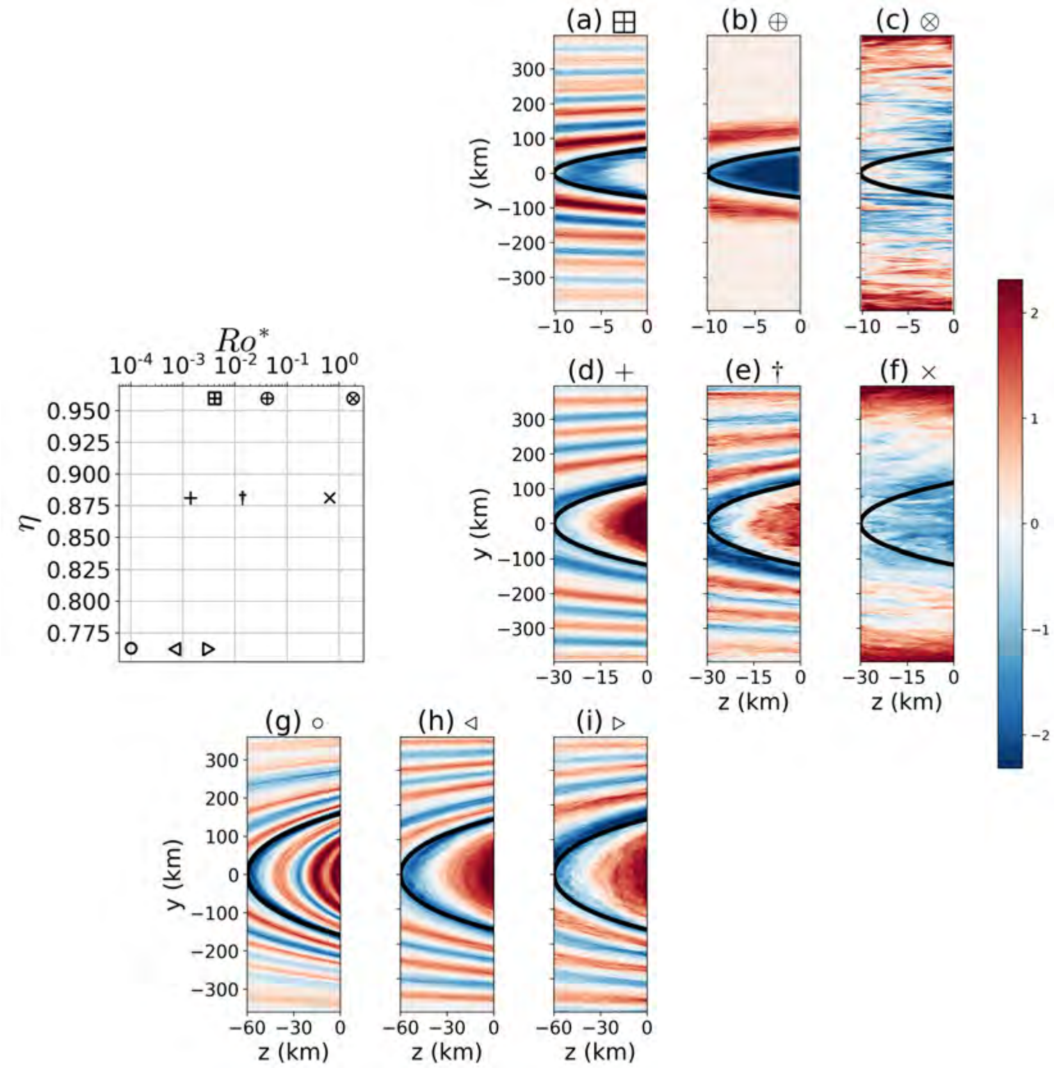

Figure 6. Instantaneous plots of standardised anomalies (see table 3) of zonal velocity at $x = 25\,\mathrm{km}$ are shown for various experiments. The first, second, and third rows represent models with η of 0.96, 0.88, and 0.76, respectively. The natural Rossby number increases towards the right for each row. The tangent cylinder is shown by thick black line.

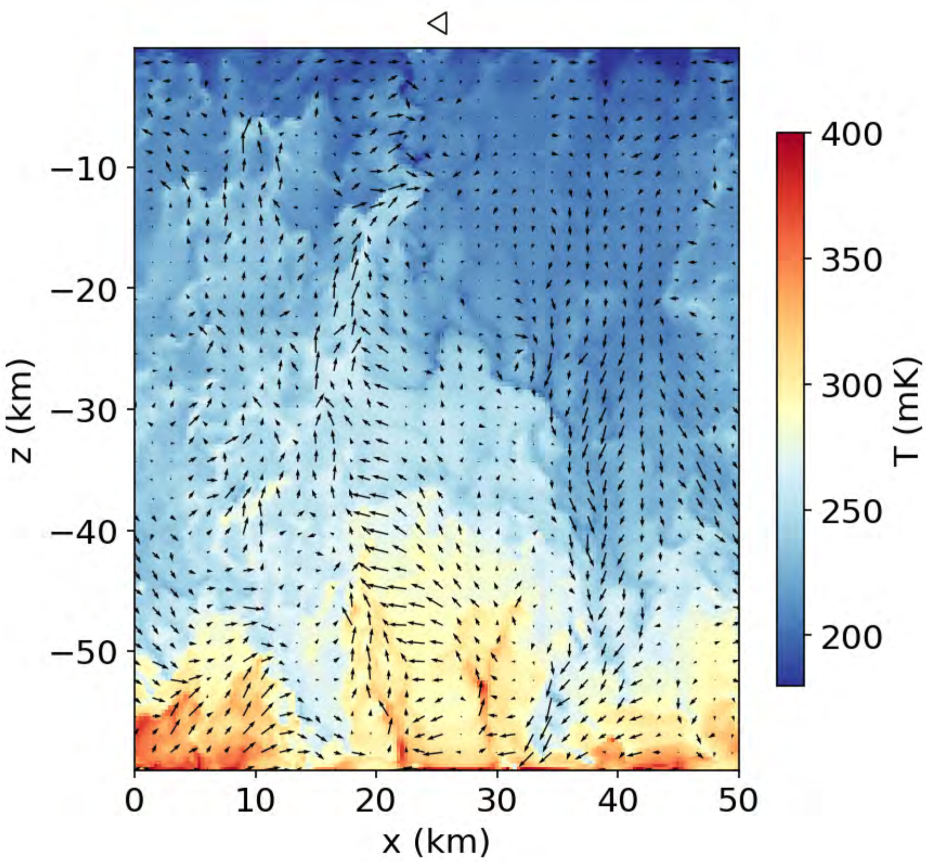

Figure 7. Instantaneous plot of temperature (shading, K) and velocity (arrows) at the equatorial xz-section is shown for experiment $\lhd$. The zonal mean of zonal velocity is subtracted to emphasize the rolls. The effect of rolls on the temperature field is obvious as the downward and upward arrows are accompanied by colder and warmer temperatures, respectively.

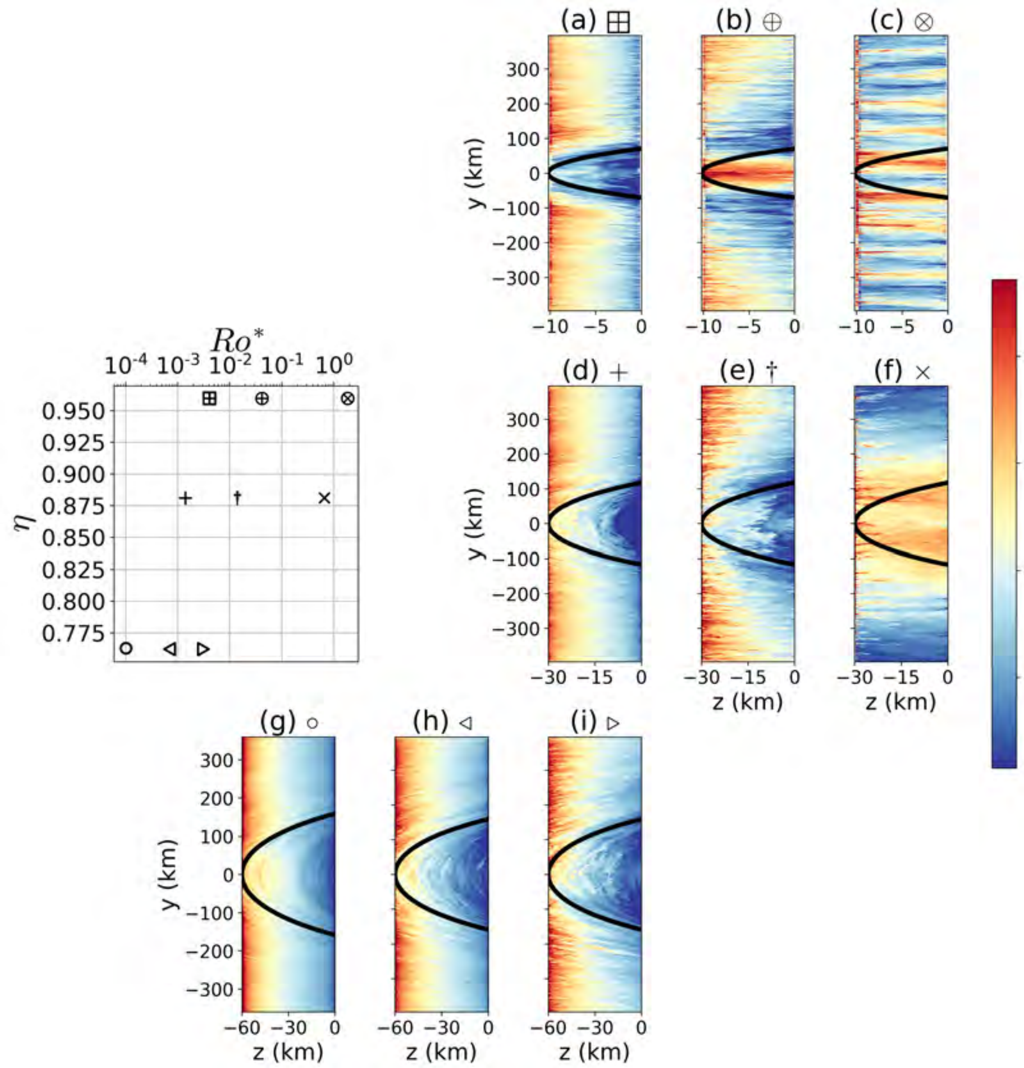

Figure 8. Instantaneous plots of standardised anomalies (See Table 3) of temperature at $x = 25$ km are shown for various experiments. The first, second, and third rows represent models with η of 0.96, 0.88, and 0.76, respectively. The natural Rossby number increases towards the right for each row. The tangent cylinder is shown by thick black line.

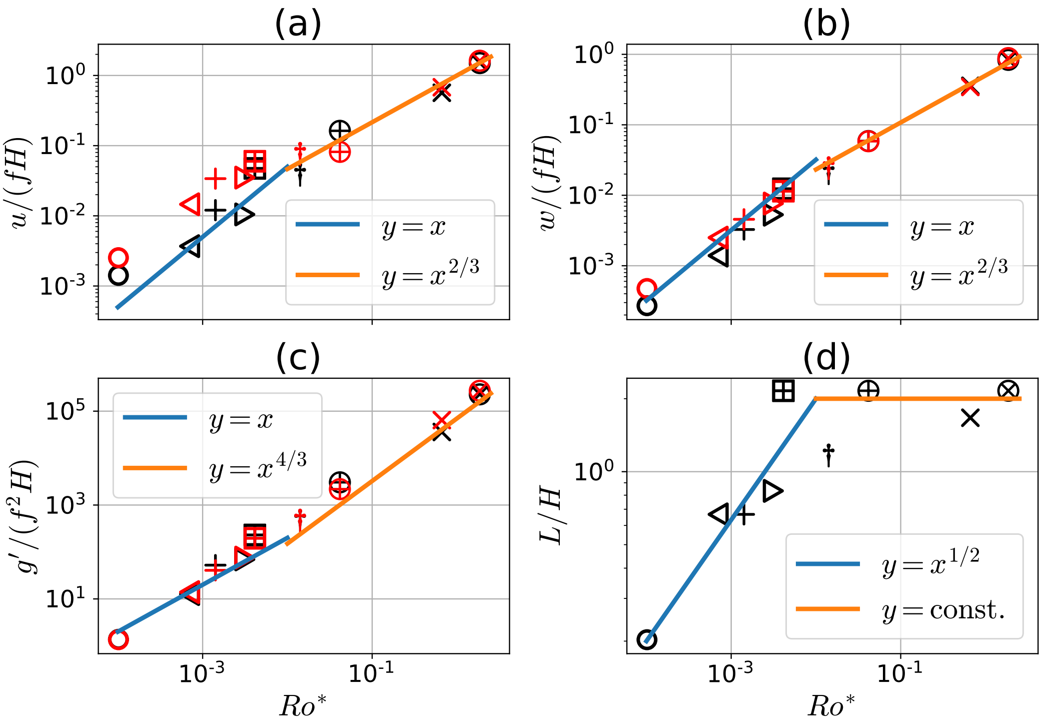

Figure 9. The black and red symbols show the normalized root mean square quantities (a: horizontal velocity, b: vertical velocity, c: buoyancy anomaly) for low and high latitudes, respectively, as functions of natural Rossby number. Root mean square quantities for low and high latitude regions are calculated between $y = 10$ and $y = 50\,\text{km}$, and $y = 200$ and $y = 300\,\text{km}$, respectively. Panel (d) shows the zonal scale of the rolls, L, normalized by the depth of the domain as a function of natural Rossby number. The blue and orange lines show the theoretical slopes for rotational and non-rotational regimes, respectively.

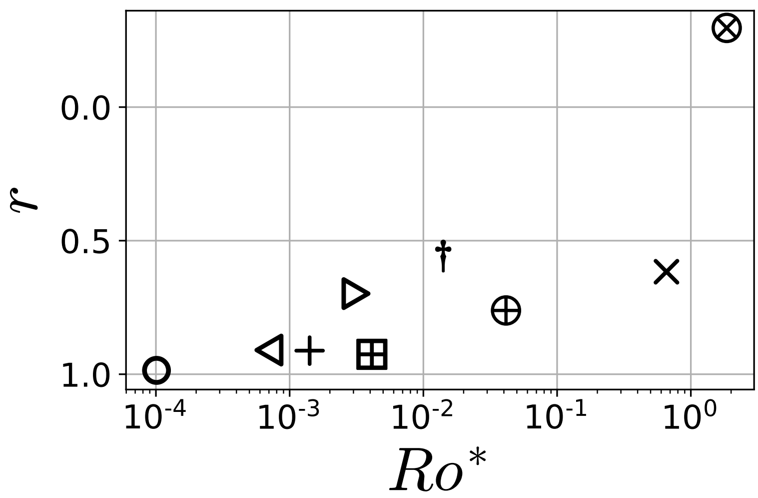

Figure 10. Tests of the zonal thermal wind equation, as measured by the correlation, r, of b with b_{TW} (Eq.15) for our experiments as a function of natural Rossby number. The top and bottom 2 km were excluded from this calculation to avoid boundary layer effects. If the correlation approaches unity then thermal wind balance is increasingly well satisfied.

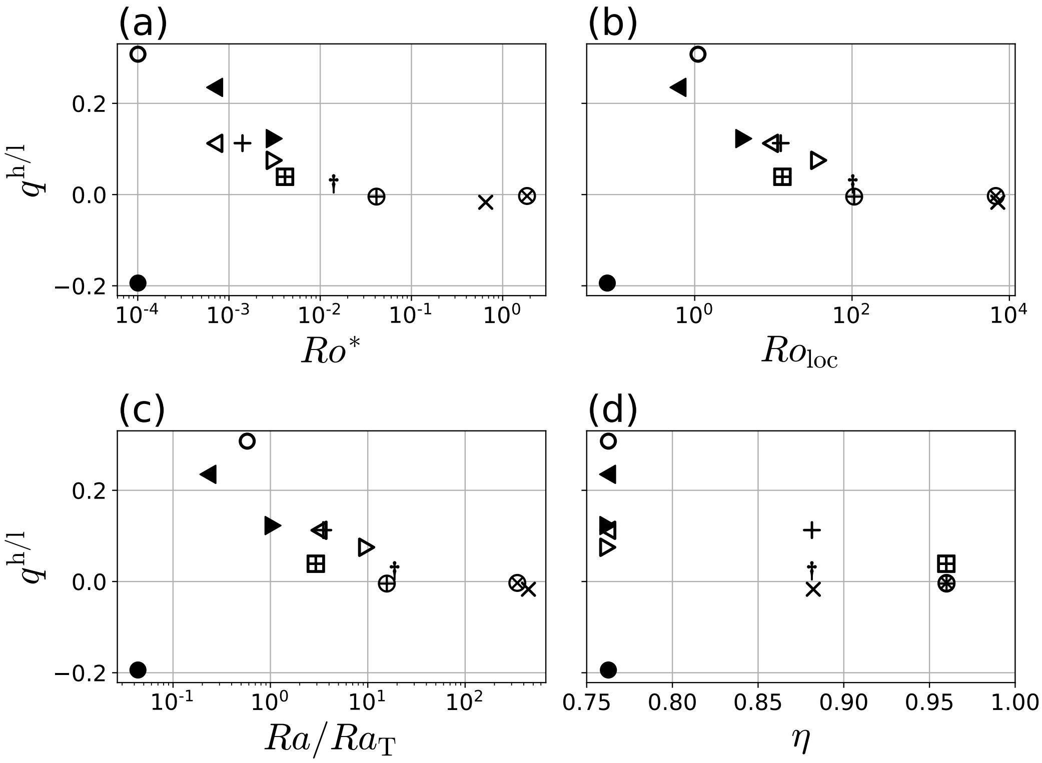

Figure 11. The ratio between high-latitude surface heat flux and low-latitude surface heat flux $q^{\mathrm{h/l}}$ from eq. (16) as a function of (a) natural Rossby number, (b) local Rossby number, (c) ratio of Rayleigh number to transitional Rayleigh number, and (d) η.

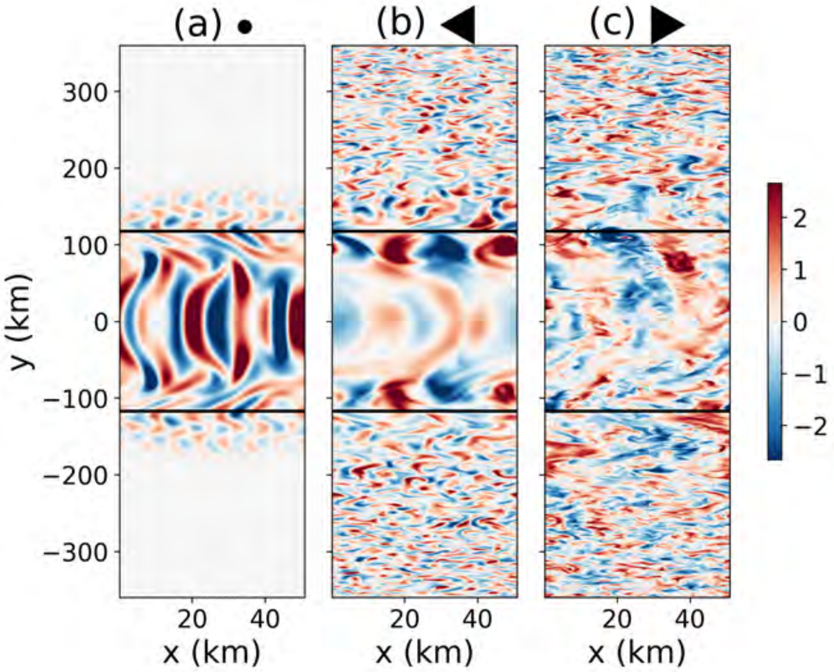

Figure 12. The normalised anomalies of vertical velocity ($(w_{\rm xy} - \bar{w_{\rm xy}})/\hat{w_{\rm xy}}$) at mid-depth for the three deep ocean experiments where we increase the viscosity and diffusivity while keeping other parameters the same. See table 2 for model setup. The mean and standard deviations for the three experiments in $\rm m\,s^{-1}$ are $\bar{w_{\rm xy}} = (5.0 \times 10^{-13}, 3.4 \times 10^{-12}, 1.7 \times 10^{-11})$ and $\hat{w_{\rm xy}} = (1.7 \times 10^{-3}, 1.5 \times 10^{-2}, 6.0 \times 10^{-2})$, respectively.

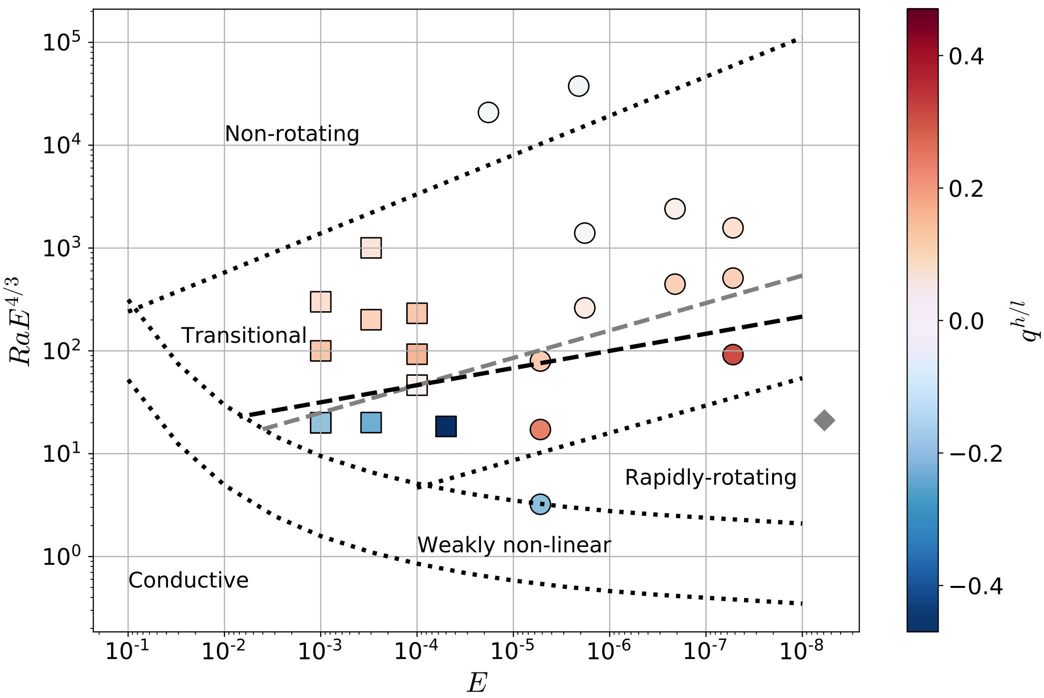

Figure 13. The y-axis represents the degree of criticality of the flow, while the x-axis represents the Ekman number. The dynamic regimes proposed by Gastine et al. (2016) are differentiated by the dotted lines and indicated by labels. The two equatorial versus polar differentiating criteria proposed by Amit et al. (2020) are shown by the black and grey dashed lines, respectively. Amit et al. (2020)'s experiments are indicated by squares. Our experiments are indicated by circles. The colors of the squares and circles indicate $q^{\mathrm{h/l}}$. Possible location of Enceladus is shown by grey diamond.

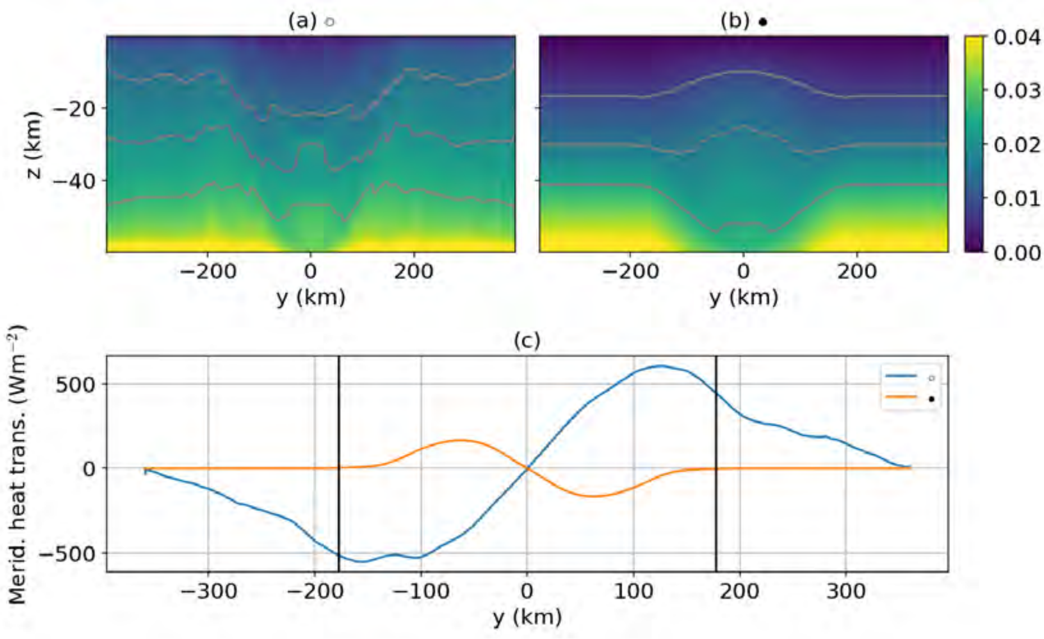

Figure 14. Panels a and b show the time and zonal mean temperature in K in experiments ○ and •, respectively. Grey lines show the 25$^{\text{th}}$, 50$^{\text{th}}$, and 75$^{\text{th}}$ percentiles. Panel c shows the meridional heat transport as a function of latitude in experiments ○ and •. The black lines show the latitudes where the tangent cylinder intersects the surface.

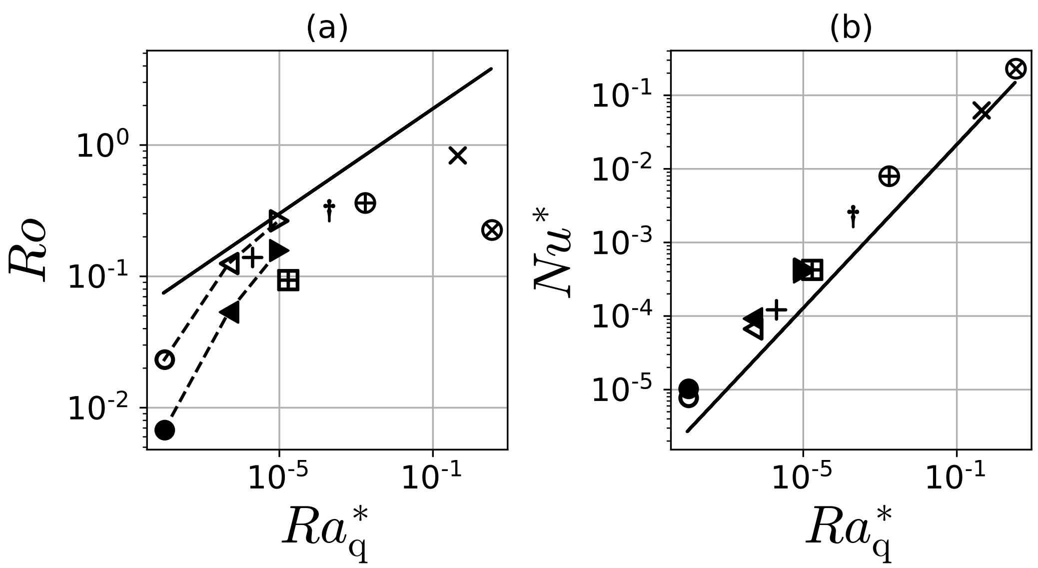

Figure B1. Values obtained from numerical Simulations are shown by markers. The theoretical asymptotic relations predicted by Christensen (2002) are represented by solid lines.